Journal of Hydrology 509 (2014) 306–319

Contents lists available at ScienceDirect

Journal of Hydrology

journal homepage: www.elsevier.com/locate/jhydrol

High-resolution characterization of a semiarid watershed: Implications on evapotranspiration estimates

Ryan C. Templeton [a], Enrique R. Vivoni [a,b,*], Luis A. Méndez-Barroso [b], Nicole A. Pierini [a], Cody A. Anderson [a], Albert Rango [c], Andrea S. Laliberte [d], Russell L. Scott [e]

[a] School of Sustainable Engineering and the Built Environment, Arizona State University, Tempe, AZ 85287, United States
[b] School of Earth and Space Exploration, Arizona State University, Tempe, AZ 85287, United States
[c] USDA-ARS Jornada Experimental Range, 2995 Knox St., Las Cruces, NM 88003, United States
[d] Earthmetrics, Brownsville, OR 97327, United States
[e] USDA-ARS Southwest Watershed Research Center, 2000 E. Allen Road, Tucson, AZ 85719, United States

ARTICLE INFO

Article history:
Received 5 April 2013
Received in revised form 5 November 2013
Accepted 23 November 2013
Available online 1 December 2013
This manuscript was handled by Konstantine P. Georgakakos, Editor-in-Chief, with the assistance of Baxter E. Vieux, Associate Editor

Keywords:
Watershed hydrology
Mixed shrubland
Environmental sensor network
Soil moisture
Evapotranspiration
Unmanned Aerial Vehicle

SUMMARY

The North American monsoon (NAM) contributes roughly half of the annual precipitation in the Chihuahuan Desert from July to September. Relatively frequent, intense storms increase soil moisture and lead to ephemeral runoff. Quantifying these processes, however, is difficult due to the sparse nature of existing observations. This study presents results from a dense network of rain gauges, soil probes, channel flumes, and an eddy covariance tower in a small watershed of the Jornada Experimental Range. Using this network, the temporal and spatial variability of soil moisture conditions and channel runoff were assessed from June 2010 to September 2011. In addition, tower measurements were used to quantify the seasonal, monthly and event-scale changes in land–atmosphere states and fluxes. Results from this study indicate a strong seasonality in water and energy fluxes, with a reduction in the Bowen ratio (B) from winter ($B = 14$) to summer ($B = 3.3$). This reduction was tied to higher shallow soil moisture (θ) availability during the summer ($\theta = 0.040$ m^3/m^3) as compared to winter ($\theta = 0.004$ m^3/m^3). Four consecutive rainfall–runoff events during the NAM were used to quantify the soil moisture and channel runoff responses and how water availability impacted land–atmosphere fluxes. The network also allowed comparisons of several approaches to estimate evapotranspiration (ET). Using a water balance residual approach, a more accurate ET estimate was obtained when distributed measurements were used, as opposed to single site measurements at the tower. In addition, the spatially-varied soil moisture data yielded a more reasonable daily relation between ET and θ, an important parameterization in many hydrologic models. These analyses illustrate the value of high-resolution sampling in small watersheds to characterize hydrologic processes.

1. Introduction

The North American monsoon (NAM) results in a pronounced increase in precipitation during the summer months of July, August, and September leading to elevated soil moisture and runoff generation in the southwest U.S. and northwest Mexico (e.g., Douglas et al., 1993; Gochis et al., 2006; Vivoni et al., 2008a). Soil moisture availability during the summer season induces rapid vegetation greening following the dry months in the spring (Salinas-Zavala et al., 2002; Watts et al., 2007; Forzieri et al., 2011). While the NAM has an annual recurrence, its seasonal precipitation amounts and its temporal distribution vary substantially from year to year. The convective nature of storm events also leads to significant rainfall variations in space and time (e.g., Gebremichael et al., 2007; Goodrich et al., 2008). Thus, it is important to have high-resolution observations to understand how watersheds will respond to storm events in terms of soil moisture changes, runoff generation and vegetation productivity during the NAM.

Soil moisture (θ) plays a critical role in partitioning energy and water fluxes in the arid and semiarid watersheds of the NAM region (e.g., Dugas et al., 1996; Kurc and Small, 2007; Vivoni et al., 2008a). Increases in soil water from summer storms result in a marked decrease in sensible heat flux and an increase in latent heat flux or evapotranspiration (ET). In addition to rainfall variations, soil moisture distributions are controlled by spatial patterns of soil, terrain and vegetation properties (e.g., Lawrence and Hornberger, 2007; Potts et al., 2010; Vivoni et al., 2010a). In

* Corresponding author. Address: School of Earth and Space Exploration, ISTB4, Building 75, Room 769, Arizona State University, Tempe, AZ 85287-6004, United States. Tel.: +1 480 727 3575; fax: +1 480 965 8102.
E-mail address: vivoni@asu.edu (E.R. Vivoni).

0022-1694/$ - see front matter © 2013 Elsevier B.V. All rights reserved.
http://dx.doi.org/10.1016/j.jhydrol.2013.11.047

regions of variable or complex terrain, redistribution processes during and after storms result in horizontal and vertical variations in soil water. These, in turn, can induce changes in how soil moisture is partitioned between evaporation from shallow soil layers and transpiration by plants from deeper layers (Scott et al., 2006; Duniway et al., 2010; Cavanaugh et al., 2011). Evapotranspiration is thus linked to the spatial distribution of soil moisture impacted by the heterogeneous landscape and its terrain, soil and vegetation characteristics.

Arid and semiarid watersheds in the NAM region are also composed of mosaics of bare soils, herbaceous plants and woody shrubs and trees. Vegetation patterns play an important role in determining infiltration, evapotranspiration losses and local runoff generation (Pierson et al., 1994; Breshears et al., 1998; Abrahams et al., 2003; Gutiérrez-Jurado et al., 2006; Mueller et al., 2007). During summer storms, overland flow is impacted by the presence of plant patches and their ability to modify soil properties, attenuate rainfall intensity and serve as runoff barriers. Thus, the spatial pattern of plant patches and bare spaces upon a heterogeneous terrain, that vary at scales on the order of meters in mixed shrubland-grassland systems (Laliberte and Rango, 2011), affects soil moisture dynamics and runoff generation (Mueller et al., 2007). These spatial features require a high-resolution characterization of terrain and vegetation properties in the hillslopes and channel reaches that compose watersheds in the NAM region (Vivoni, 2012a).

Spatiotemporal changes in vegetation distributions are also commonly observed in the arid and semiarid watersheds of the region (e.g., Huxman et al. 2005; Newman et al. (2006a)), in response to grazing, fire and climate pressures. Areas experiencing woody plant encroachment are characterized by increasing amounts of woody shrubs and trees with respect to herbaceous cover. In these settings, desertification processes promote further establishment of woody plants, an increase in bare soil and a reduction in grasses, leading to a more heterogeneous mosaic of surface properties (Gibbens et al., 2005; Okin et al., 2009; Browning et al., 2012). Vegetation changes can lead to a myriad of hydrologic consequences at individual sites that together affect local watershed dynamics as well as downstream areas. For example, Bestelmeyer et al. (2011) postulate that woody plant encroachment in upland sites has differential effects on the vegetation conditions downstream depending on the degree of hydrologic connectivity. In areas where bare soils are well connected along a terrain gradient (Mueller et al., 2007), the authors expect that vegetation changes affect downstream hydrologic conditions. Peters et al. (2010) also postulate that grass establishment is enhanced under scenarios of increased NAM rainfall at downstream sites that benefit from upland water redistribution in a heterogeneous landscape.

Clearly, a spatially-explicit approach is required to capture hydrologic connectivity in arid and semiarid watersheds in a way that allows examining the impact of vegetation changes on downstream conditions. In this study, we take a step towards developing such an approach through the establishment of high-resolution observations in a small watershed in southern New Mexico, USA. An environmental sensor network in a Chihuahuan Desert mixed shrubland was designed to capture storm event transformation into spatially-variable soil moisture and runoff responses in a watershed where terrain and vegetation gradients are observed from the use of high-resolution imagery from an Unmanned Aerial Vehicle (UAV). In particular, the UAV products allow characterizing the terrain attributes (i.e., elevation, slope, aspect, upstream area) and vegetation species distributions used to interpolate local site measurements from the environmental sensor network to the entire watershed area. Using the observations, we quantify the temporal dynamics of water and energy fluxes in the watershed at the seasonal, monthly and storm event scales and provide insight into their spatial variations and their linkage.

We also determine the role of watershed-scale soil moisture conditions on the estimation of evapotranspiration (ET) to quantify the value of high-resolution observations as compared to traditional approaches using a more limited number of soil moisture profiles (e.g., Scott, 2010). This is performed using two approaches: (1) as a residual of the monthly water balance ($ET = P - Q - \Delta S/\Delta t$, where P is precipitation, Q is runoff, and $\Delta S/\Delta t$ is the change in soil water storage over time), and (2) as a result of a piecewise linear relation between ET and θ. We postulate that a set of high-resolution observations is required to properly characterize the hydrologic dynamics in the semiarid watershed due to its variable terrain and vegetation distributions, as observed from UAV imagery. Furthermore, the observations may aid in understanding how the watershed underwent a transition from a grassland to a mixed shrubland over the last century (Gibbens et al., 2005) and how this might be related to hydrologic connectivity.

2. Methods

2.1. Study watershed and its characterization

The study area is in a shrub-dominated portion of the San Andres Mountain piedmont, along the southeastern boundary of the Jornada Experimental Range (JER) in southern New Mexico, USA (Fig. 1). A small watershed (4.67×10^4 m^2 or 4.67 ha) in the alluvial slope or bajada was first instrumented with a rain gauge and runoff flume in 1977. Using these records, Turnbull et al. (2013) analyzed the aggregate relation between event rainfall and runoff over 1977–1985 and 2003–2011, finding a change attributed to variations in precipitation intensity. Over this period, however, the topographic, vegetation and channel characteristics in the watershed also likely varied (e.g., Gibbens et al., 2005; Monger and Bestelmeyer, 2006). In addition to these long-term changes, the watershed has seasonal variations related to the NAM (July–September), which accounts for ~60% of the annual rainfall of 308 mm as obtained over the period 2005–2010 at the site rain gauge. Fig. 2 illustrates this seasonality through the monthly mean rainfall and its standard deviation (std) and the resulting vegetation response through the monthly mean (and std) Normalized Difference Vegetation Index (NDVI).

Our high-resolution observational efforts commenced in 2010 with the installation of an environmental sensor network and the characterization of the watershed through detailed field sampling and UAV-based image analysis. For example, Fig. 1 shows the location of the channel network mapped with a differential global positioning system (dGPS, Leica Geosystems GPS 1200). The watershed boundary in Fig. 1 was derived from a 1 m digital terrain model (DTM) derived from UAV images at a height of 200 m in October 2010. The BAT 3 (MLB Co.) UAV mounted with a Canon SD 900 digital camera was used to create a 6 cm orthomosaic of overlapping photos (75% forward lap and 40% side lap) shown in Fig. 1. Orthorectification and DTM generation were accomplished using the methods of Laliberte et al. (2008) and Laliberte and Rango (2011). An analysis of the DTM revealed the major terrain features in the watershed, including the distributions of elevation, slope and aspect, as shown in Fig. 3. Three major areas (north-, south- and west-facing hillslopes) with low to moderate slopes (~0–6°) are present in the watershed (mean slope of 2.6°), while the channel banks and propagating channel heads have higher slopes (~15–25°). In Fig. 3d, three sub-watersheds delineated upstream of the channel flumes are shown, with areas ranging from 0.77 ha (Flume 1) to 1.31 ha (Flume 3).

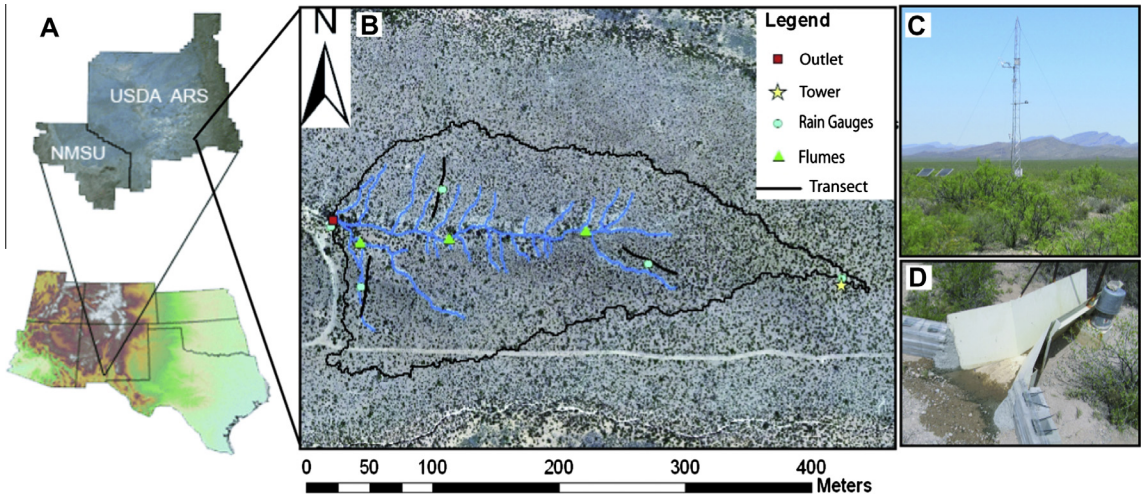

Fig. 1. A. Location of the study watershed in the United States Department of Agriculture – Agricultural Research Service (USDA-ARS) Jornada Experimental Range near Las Cruces, New Mexico. This is located next to the New Mexico State University (NMSU) Chihuahuan Desert Rangeland Research Center. B. Watershed representation including: 6 cm aerial color image obtained from the UAV, watershed boundary upstream of the outlet flume derived from a 1 m DTM, channel network delineation from a dGPS survey, and environmental sensor network locations (Tower, Rain Gauges, Flumes, Transects). C. Eddy covariance tower. D. Small flume in the interior of the watershed. (For interpretation of the references to colour in this figure legend, the reader is referred to the web version of this article.)

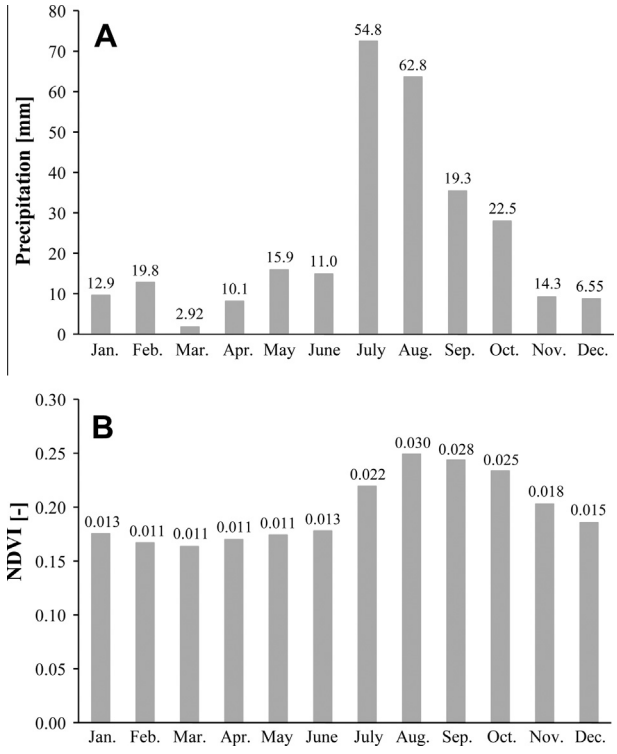

Fig. 2. A. Monthly mean precipitation (2005–2010) at site rain gauge (TB3, Hydrological Services). B. Monthly mean NDVI (2005–2010) from 250 m, 16 day resolution Moderate Resolution Imaging Spectroradiometer (MODIS) sensor. NDVI is dimensionless. Numerical values on top of each bar represent the monthly standard deviation (std) over the period.

The UAV imagery from the Canon SD 900 digital camera was also used to derive a vegetation species classification based on the Red, Green, and Blue (RGB) spectrum signature of individual patches, using the methods of Laliberte et al. (2012), as shown in Fig. 4 (the inset also shows a photograph of the BAT 3 UAV). Table 1 presents the areal coverage of the major classes in the watershed, indicating a dominance of bare soil (66%), followed by four shrub species (mariola, mesquite, creosotebush and tarbush) and a low fraction of herbaceous cover (5%). The classification map in Fig. 4 was field verified through random sampling, indicating an overall accuracy of 95% at the major class level and 89% at the species level. In addition, the Line-point Intercept method (Canfield, 1941; Herrick et al., 2009) was used in May 2010 along three 70 m transects on each hillslope, leading to ~61% bare soil and 77% of the vegetated areas occupied by the four major shrubs, in close agreement with Table 1. Soil characteristics were sampled in the watershed at multiple sites in the hillslopes up to a depth of 50 cm, revealing a loam soil texture (37.4% sand, 41.8% silt, 20.8% clay), a bulk density of 1.37 g/cm^3, and a surface layer with gravels and fine cobbles, consistent with Monger (2006). An indurated calcium carbonate ($CaCO_3$) or caliche horizon was found between 0 cm in the channels and 60 cm at upper elevations, with an average depth of ~40 cm. Channels incise into the caliche layer at upper elevations leading to impermeable bottoms, while coarse sands and gravels occupy the channel cross-sections at downstream sites near the watershed outlet.

2.2. Environmental sensor network and data processing

The distributed observations in the study watershed consisted of rainfall, soil moisture, soil temperature and channel runoff sensors along with an eddy covariance (EC) tower, as shown in Fig. 1 and described in Table 2. Four tipping-bucket rain gauges (TE525MM, Texas Electronics), mounted at 1 m above the ground surface and calibrated over a wide dynamic range of precipitation intensities, were placed in the three major hillslopes (at the center of transects measuring soil moisture and temperature) and at the most distant point from the outlet, near the EC tower. A fifth rain gauge (TB3, Hydrological Services) had been in operation at the outlet since 2005. Due to sporadic failures of the EC tower and outlet rain gauge, the three interior gauges were used to estimate spatially-averaged precipitation rates using Thiessen polygons within the watershed boundary derived from the UAV-based DTM, with areal weights of 0.22, 0.33 and 0.44 for R2, R3 and R4 (Table 2). As the rain gauges measured individual tips, precipitation amounts were estimated at a range of durations, from 1 to 30 min intervals.

The three soil moisture and temperature transects were strategically located to sample the north-facing (transect 1 or T1), south-facing (T2), and west-facing hillslopes (T3). Vegetation was fairly

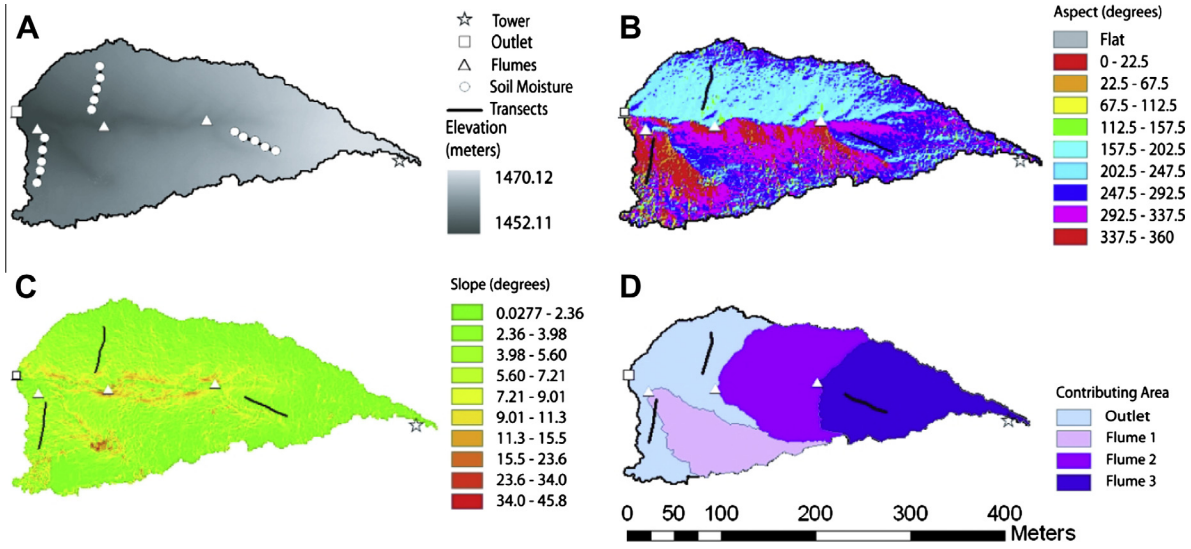

Fig. 3. A. Watershed elevation (m) and sensor locations. B. Aspect (degrees from north). C. Slope (degrees). D. Non-overlapping sub-watershed areas upstream of each flume.

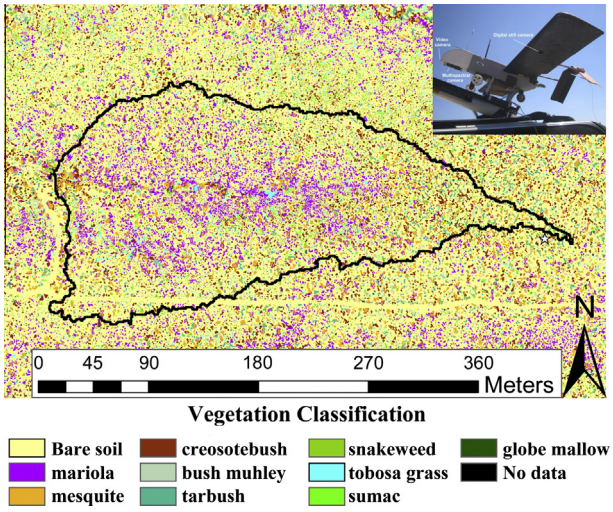

Fig. 4. Spatial distribution of vegetation types following classification described in Table 1. Inset shows the UAV BAT3.

Table 1
Watershed vegetation and bare soil classification in percentage of area (4.67×10^4 m^2).

Classification	Areal coverage (%)
Bare soil	65.95
Parthenium incanum (mariola)	11.94
Prosopis glandulosa (mesquite)	6.47
Larrea tridentata (creosotebush)	5.82
Muhlenbergia porteri (bush muhley)	2.89
Flourensia cernua (tarbush)	2.48
Gurierrezia sarothrae (snakeweed)	1.82
Pleuraphis mutica (tobosa grass)/*Sporobolus sp.* (Dropseed)	1.40
Rhus sp. (sumac)	1.15
Sphaeralcea angustifolia (globe mallow)	0.04
No data	0.02

consistent among the transect locations, representing well the distribution of bare soil and vegetation types in the basin (Fig. 4), with a dominance of *Parthenium incanum* (mariola), *Prosopis glandulosa* (mesquite) and *Larrea tridentata* (creosotebush). Each transect consisted of 15 soil dielectric sensors (Hydra Probe, Stevens Water) with five profiles of three sensors (5, 15 and 30 cm depths) placed from near the main channel to 50 m upslope at 10 m intervals (Fig. 3a). One site only had two sensors due to the shallow nature of the $CaCO_3$ horizon at 20 cm. The sensors measure the impedance of an electric signal through the soil sampling volume, following Campbell (1990), to determine the volumetric water content or soil moisture (θ) in m^3/m^3 and the soil temperature (T_s) in °C. A 'loam' factory calibration equation was used in the conversion (Seyfried et al., 2005) and verified with gravimetric measurements (θ_g) over a range of values from 0.03 to 0.37 m^3/m^3 ($\theta = 0.98\theta_g + 0.01$, $R^2 = 0.97$). Half-hourly averaged soil moisture and temperature data were recorded for all transect locations. Spatially-averaged θ and T_s were estimated by using elevation and aspect at each site (see contributions in Table 2) to represent similar areas in the watershed, leading to 15 categories (Templeton, 2011).

Four channel flumes in the watershed were used to measure runoff. The outlet structure (F4) is a 2.8 m^3/s Santa Rita supercritical flume installed in 1977 (Smith et al., 1981), while the three interior supercritical flumes (F1, F2, F3) are smaller (Wainwright et al., 2002). In each flume, gauge pressure data from a pressure transducer (CS450, Campbell Scientific) in the stilling well were obtained at 1 min intervals. An in situ linear calibration was performed for each flume to relate water height (h in cm) to pressure differential measurements (p in mV) in the form of $h = mp + b$. Channel runoff (Q in m^3/s) at the outlet flume was estimated as $Q = 0.081h + 4.307h^2$ (Smith et al., 1981; Turnbull et al., 2013), while runoff in the interior flumes was obtained by applying the ISO 4359 (1983) iterative procedure using the flume dimensions and measured water height (see Templeton, 2011, Appendix F). Runoff data quality control also included separation of individual hydrographs, rescaling to account for sensor drift and temperature effects, and removal of spurious readings related to sporadic sediment buildup.

A 10 m eddy covariance tower (T0) was used to characterize radiation, energy and water fluxes as well as meteorological and soil conditions on a flat surface at the eastern boundary of the watershed (Fig. 1). Tower sensors included a net shortwave and longwave radiometer at 5 m height (CNR2-L, Kipp & Zonen), a pyranometer at 5 m (CMP3-L, Campbell Scientific), a three-dimensional sonic anemometer (CSAT3, Campbell Sci.) and an open-path Infrared Gas Analyzer (LI7500, Li-COR Biosciences) aligned to the

Table 2
Environmental sensor network characteristics, including sensor type, ID, geographic location (UTM 13 N, WGS84), elevation, aspect, slope and areal contributions. Contributions represent the elevation-aspect regions (soil probes), Thiessen polygon areas (rain gauges) and the non-overlapping, upstream sub-watershed areas (flumes).

Sensor type	ID	Northing (m)	Easting (m)	Elevation (m)	Aspect (deg)	Slope (deg)	Contribution (%)
Soil probe	SM1	3606431.75	349156.52	1453.61	329.75	5.40	3.10
	SM2	3606418.72	349154.27	1454.85	322.07	3.05	2.40
	SM3	3606406.58	349153.37	1455.85	305.93	6.34	2.64
	SM4	3606396.69	349152.03	1456.82	352.44	3.41	2.89
	SM5	3606384.10	349148.88	1457.34	216.06	2.77	34.08
	SM6	3606461.42	349205.97	1456.04	197.79	7.62	6.10
	SM7	3606471.31	349208.67	1456.88	207.96	4.24	2.33
	SM8	3606483.00	349211.36	1457.64	203.46	3.97	2.81
	SM9	3606494.69	349214.96	1458.62	221.29	6.33	2.74
	SM10	3606507.27	349214.96	1459.04	260.96	2.66	19.69
	SM11	3606437.60	349356.56	1462.21	296.33	5.51	2.14
	SM12	3606432.20	349366.00	1462.89	265.49	3.61	1.15
	SM13	3606428.16	349377.69	1463.66	253.34	4.28	1.34
	SM14	3606421.41	349388.92	1464.36	259.98	5.65	1.85
	SM15	3606417.82	349400.16	1465.02	288.49	2.14	14.76
Rain gauge	R1	3606454.23	349126.40	1452.51	18.23	2.32	0
	R2	3606407.93	349150.23	1455.80	5.50	3.96	22.13
	R3	3606483.45	349214.51	1457.77	186.66	5.45	33.45
	R4	3606425.46	349377.24	1463.61	187.96	8.74	44.42
	R5	3606414.67	349530.97	1469.47	319.45	2.86	0
Flume	F1	3606441.64	349149.33	1453.00	14.95	4.29	16.58
	F2	3606444.34	349219.00	1455.00	260.54	3.45	27.29
	F3	3606451.08	349328.24	1459.61	210.46	3.60	28.04
	F4	3606455.58	349126.85	1452.52	30.94	1.71	28.09
Tower	T0	3606407.79	349528.84	1469.40	228.60	0.22	–

dominant southwest wind direction at 7.1 m height, air temperature and humidity at 3.4 m (HMP45C, Campbell Sci.), two soil heat flux plates at 8 cm depth in bare soil and vegetated areas (HPF01-SC, Hukseflux) with thermocouples at 2 and 4 cm (TCAV-L, Campbell Sci.) and soil water content reflectometers (CS616, Campbell Sci.) at 5, 15, 30 and 50 cm depths, verified with gravimetric samples ($\theta = 1.06\theta_g + 0.02$, $R^2 = 0.97$). Covariances of vertical wind speed, temperature and water vapor concentration were calculated at 20 Hz and processed to obtain sensible (H) and latent heat (λE) flux at 30 min intervals using EdiRe (University of Edinburgh). Flux corrections for the EC measurements followed Scott et al. (2004) and included data filtering to remove periods with rainfall and equipment malfunction, despiking of periods above +3 standard deviations of the monthly mean, the Webb method for density correction (Webb et al., 1980), the Monin–Obukhov method for stability (Foken, 2006) and coordinate plane rotation (Wilczak et al., 2001). Gap filling using linear interpolation was applied to short 30-min periods of no data or where extreme flux values were filtered. Long periods (>2 h) of missing data (see Table 2 in Templeton, 2011) were excluded from the analysis. Ground heat (G) flux was calculated using the two heat flux plates with overlying soil thermocouples and a water content reflectometer at 5 cm. Heat flux data from the two plates was averaged using the areal cover of bare soil and vegetation (Table 1).

2.3. Water and energy balance estimates

The water and energy states and fluxes in the watershed were computed at daily, monthly and annual scales during the period of June 1, 2010 to September 30, 2011 (487 days) using:

$$\frac{\Delta S}{\Delta t} = P - ET - Q \pm e, \text{and} \tag{1}$$

$$R_n = H + \lambda E + G \pm \varepsilon, \tag{2}$$

where S is the soil water storage (mm), R_n is net radiation or the sum of net shortwave (SW) and longwave (LW) components (W/m^2) and e and ε are error terms. S was obtained as the weighted depth-average of θ measurements and converted using $S = \theta d$, where d is the soil depth. We compared estimates of S based on: (1) single measurements at the tower site with depth weights of 0.17, 0.17, 0.33 and 0.33 at 5, 15, 30 and 50 cm, respectively, and $d = 60$ cm, and (2) distributed measurements in the watershed from the 15 soil profiles (Fig. 3a) with depth weights of 0.25, 0.25 and 0.5 at 5, 15 and 30 cm, respectively, and $d = 40$ cm. When using the single site ΔS data collected near the tower, monthly ET_{single} was obtained as a residual of the water balance using the monthly outlet runoff (Q) and the monthly precipitation (P) at the tower rain gauge. When using the distributed measurements, monthly ET_{basin} was obtained as the water balance residual using a weighted spatial average of monthly P and ΔS, using weights shown in Table 2 derived from the UAV-based DTM (Templeton, 2011), and monthly Q at the outlet. Both estimates are compared to the in situ EC measurements (ET_{EC}) treated as the ground-truth. For periods when EC equipment failure occurred (24% of total days), the Hargreaves method was used to gap-fill the daily estimates with ET_o (mm/day) as:

$$ET_o = 0.0135 K_t I_e T_d^{0.5} (T_c + 17.8), \tag{3}$$

where K_t is an empirical coefficient determined as 0.195 (wet days) and 0.0184 (dry days) for the site, I_e is extraterrestrial solar radiation in the same units as evapotranspiration (mm/day), T_d is the difference between daily maximum and minimum air temperature (°C), and T_c is the average daily air temperature in °C (Hargreaves and Samani, 1982, 1985). K_t values were regressed from periods with available EC data for wet and dry days based on a threshold in the spatially-averaged soil moisture of 0.1 m^3/m^3.

A second approach for assessing the value of the high-resolution data was based on a piecewise linear relation of daily ET and soil moisture (Rodríguez-Iturbe and Porporato, 2004):

$$ET(\theta) = \begin{cases} 0 & 0 < \theta \leqslant \theta_h \\ E_w \frac{\theta - \theta_h}{\theta_w - \theta_h} & \theta_h < \theta \leqslant \theta_w, \\ E_w + (ET_{max} - E_w) \frac{\theta - \theta_w}{\theta^* - \theta_w} & \theta_w < \theta \leqslant \theta^* \\ ET_{max} & \theta^* < \theta \leqslant \varphi \end{cases} \tag{4}$$

where E_w is soil evaporation, ET_{max} is the unstressed, maximum evapotranspiration, θ_h, θ_w and θ^* are the hygroscopic, wilting and plant stress soil moisture thresholds, and ϕ is the soil porosity. Vivoni et al. (2008a) used this relation as a method of regressing *ET* and θ observations, based on a nonlinear optimization algorithm of Gill et al. (1981), to characterize the observed linkage. The optimization algorithm fits Eq. (4) to pairs of daily values of *ET* and θ by sampling over specified ranges of parameter values (E_w, ET_{max}, θ_h, θ_w, θ^* and ϕ). The goodness of fit is assessed with respect to the *ET*-θ data utilizing the mean absolute error (MAE in mm/day). Of particular interest is that relations such as $ET = f(\theta)ET_{max}$ are important parameterizations in a wide range of hydrology models (e.g., Chen et al., 1996; Ivanov et al., 2004). Here, the depth-averaged θ from two sources is related to measured *ET* from the EC method (ET_{EC}): (1) single measurements at the tower site, and (2) the spatial average of distributed measurements at the 15 soil profiles in the watershed using the weights in Table 2. After parameter estimation (E_w, ET_{max}, θ_h, θ_w, θ^* and ϕ) and the evaluation of the fit from the optimization algorithm from each source, the established *ET*-θ relation was used to directly estimate daily *ET* from either site or distributed θ measurements and tested against the daily observed ET_{EC} as a validation. Thus, the approach is to use the single site or distributed soil moisture data to calculate daily *ET* once the *ET*-θ relation has been derived. This comparison is useful to conduct since the piecewise linear relation does not capture the entire variability in daily *ET*.

3. Results and discussion

3.1. Seasonal variability of spatially-averaged watershed dynamics

The seasonal variability of water and energy states and fluxes are shown in Fig. 5. The two summers exhibit higher rainfall amounts (119 and 112 mm in 2010 and 2011), increases in soil moisture at all depths, channel runoff at the watershed outlet, and higher soil temperatures at all depths, as compared to the fall, winter and spring seasons. We defined the seasons as summer (July 1 to September 30), fall (October 1 to December 31), winter (January 1 to March 31) and spring (April 1 to June 30). The uppermost soil layer (5 cm) had large increases in soil moisture in response to storms and rapid recessions during interstorm periods, as characteristic of the Chihuahuan Desert (e.g., Kurc and Small, 2007; Gutiérrez-Jurado et al., 2007). Shallow soil moisture averaged during the summer ($\theta = 0.040\ m^3/m^3$) was an order of magnitude higher than in the winter season ($\theta = 0.004\ m^3/m^3$). The upper soil layers also had the largest diurnal variations in soil temperature, which decreased substantially after summer rainfall events. Temporal changes in soil moisture and temperature at 15 and 30 cm were dampened and showed an increasing lag in response time with soil depth relative to rainfall occurrence. Interestingly, deeper soil layers remained wetter than the surface soils during interstorm periods lasting more than a week in the summer and throughout the entire duration of the other seasons. The low soil moisture response at 30 cm above the caliche layer indicates that limited recharge occurs at that soil depth, except during the summer, for the study period analyzed. As a result, it is possible that soil moisture enters into the $CaCO_3$ horizon in the summer season where it is stored and released slowly during the rest of the year, as discussed by Duniway et al. (2010).

Turbulent heat fluxes at the eddy covariance tower are representative of a time-variable footprint with an area around the site of ~23,400 m^2 (2.34 ha) throughout the year, based on an analysis of the 50% source area using the footprint model of Kormann and Meixner (2001). Both sensible (*H*) and latent heat (λE) fluxes show strong seasonal variations linked with both energy and water availability (Fig. 5b). As a result, the mid-day Bowen ratio ($B = H/\lambda E$) decreases from winter ($B = 14$) to summer seasons ($B = 3.3$). Sensible heat flux exhibits maximum values during the spring and early summer (~500 W/m^2 for peaks of 30 min intervals), coincident with rising soil temperatures at all depths. Upon the NAM onset, *H* decreases after storm events (~300 W/m^2) as more available energy is consumed by latent heat fluxes derived from soil evaporation and plant transpiration from evergreen and deciduous shrubs and herbaceous cover. During short periods of high soil moisture in the summer season, λE at 30 min intervals can reach ~250 W/m^2 and exceed the magnitude of sensible heat flux. Higher evapotranspiration rates are primarily responsible for soil moisture decreases observed at 5 and 15 cm after individual storm events and for recessions lasting into the fall season. In the fall, winter and spring,

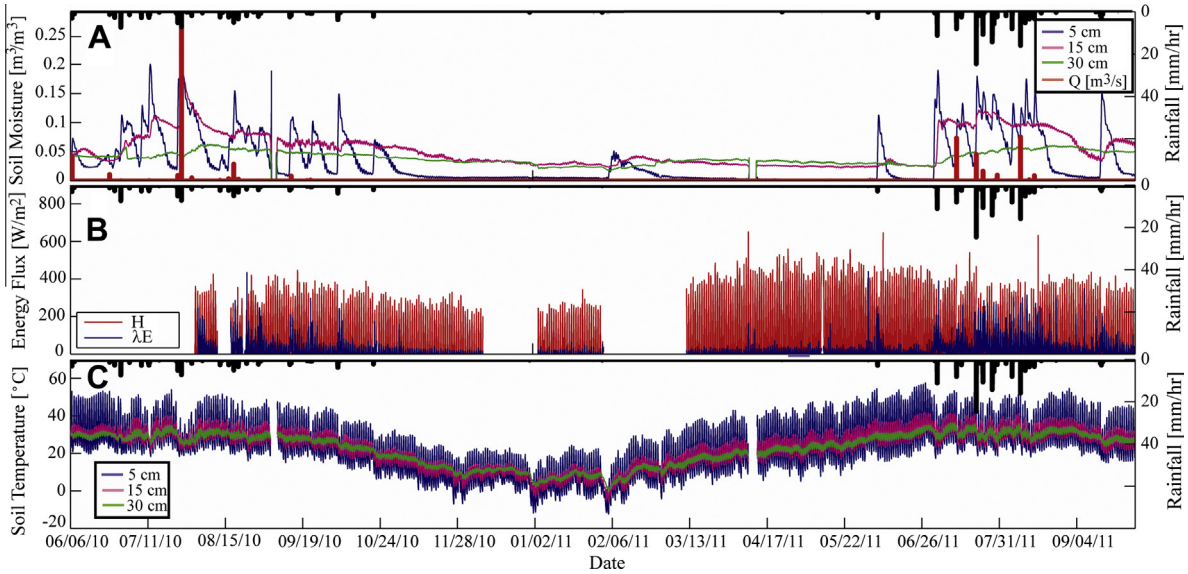

Fig. 5. A. Spatially-averaged soil moisture (m^3/m^3) at 5, 15 and 30 cm depths and channel outlet runoff (Q in m^3/s on left hand axis). B. Latent and sensible heat flux (W/m^2) at the eddy covariance tower. C. Spatially-averaged soil temperature (°C) at 5, 15 and 30 cm depths. Spatially-averaged rainfall (mm/h) obtained from Thiessen polygons of rain gauge sites (Table 2) is shown in all cases. All data at 30 min intervals and gaps indicate periods of data loss. The spatial averaging of soil moisture and temperature was performed using elevation-aspect regions (Templeton, 2011). Contributions from each probe to the spatial average are shown in Table 2.

low λE rates (~20–60 W/m^2), likely from evergreen shrub transpiration, are sustained from slowly-receding soil moisture present in deeper layers (15 and 30 cm) since the uppermost soil is dry.

Fig. 6 presents the seasonally-averaged diurnal variability of energy fluxes during the study period at the tower. Incoming solar (I_s) and net radiation (R_n) both exhibit maximum values in the spring and summer, followed by the fall and winter seasons. Sporadic cloud cover results in lower I_s in the summer as compared to spring with a difference of ~150 W/m^2 at local noon. Nevertheless, R_n is nearly equal in the spring and summer (~600 W/m^2) due to variations in *SW* and *LW* radiation induced by albedo and soil temperature variations. These values are consistent with summer measurements by Dugas et al. (1996) for a creosotebush site at the JER. Net radiation in the spring and summer seasons exceed values in the fall and winter by ~160 W/m^2. The partitioning of R_n into sensible, latent and ground heat flux varies seasonally according to the soil moisture and temperature conditions and the vegetation phenology. *H* is the dominant turbulent energy flux during the year accounting for 51% (summer) to 84% (winter) of monthly total R_n, while λE has values ranging from 5% (winter) to 32% (summer) of R_n. Daily-averaged summer λE values (~100 W/m^2) are also similar to measurements during a dry day (August 20, 1991) by Dugas et al. (1996) at their creosotebush site. Ground heat flux accounts for a large percentage of day-time R_n in the summer and fall (~200 W/m^2), but decreases substantially in the winter and spring as soil temperature and soil moisture are reduced. Energy balance errors (ε) arising from the independent observations varied from +10% to 15% of R_n at the monthly scale (Templeton, 2011), in a range consistent with measurements at other semiarid sites (Scott, 2010).

Seasonal variations of energy and water fluxes should be related to species-specific phenological changes in the mixed shrubland watershed (Vivoni, 2012a). In addition to inspecting the spatially-averaged NDVI (Fig. 2b) from satellite remote sensing, we infer vegetation changes through the seasonal variations in surface albedo at the eddy covariance tower. Surface albedo varies in accordance with vegetation greening (e.g., Watts et al., 2007). Fig. 7 shows the diurnal variability of albedo (a), obtained as $a = 1 - SW/I_s$, averaged for each season. The mid-afternoon albedo decreases in response to summer greening of shrubs and grasses,

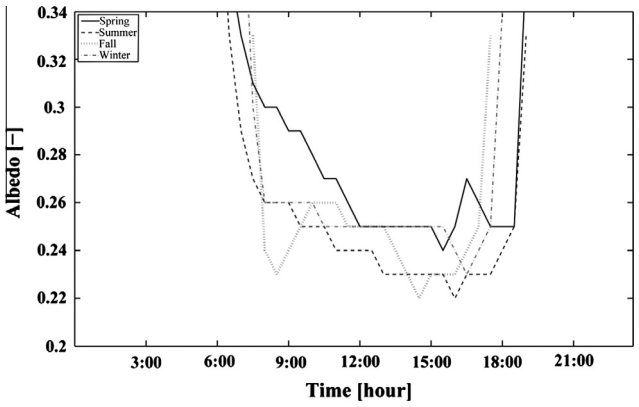

Fig. 7. Seasonally-averaged diurnal variation of albedo with the seasons defined as in Fig. 6.

from values of 0.25 in winter and spring to 0.23 for the summer and fall seasons. These estimates are based on spatial averages in the radiometer field of view that includes individual shrubs as well as a large percentage of bare soil, matching the conditions in the watershed. While these values are consistent with prior measurements at the JER (e.g., Barnsley et al., 2000), the link between species-specific phenology and surface albedo is not presently possible at the scale of the radiometer footprint, though efforts by Browning et al. (2009) may help to address this.

3.2. Monthly water and energy balance components in the watershed

The monthly variation in the water and energy balance components is shown in Fig. 8 for the period with the best available data in the watershed. Precipitation (P) followed the seasonal progression expected for the NAM region, but with drier than average fall, winter and spring seasons (Fig. 2a). Thus, the sharp increase in P during the summer leads to an abrupt increase in available soil water. Evapotranspiration (ET) was the dominant mechanism for soil water losses, accounting for 138% of P over this period due to three reasons: (1) the potential for precipitation undercatch at the rain gauge sites (Larson and Peck, 1974), assumed to be 5% of

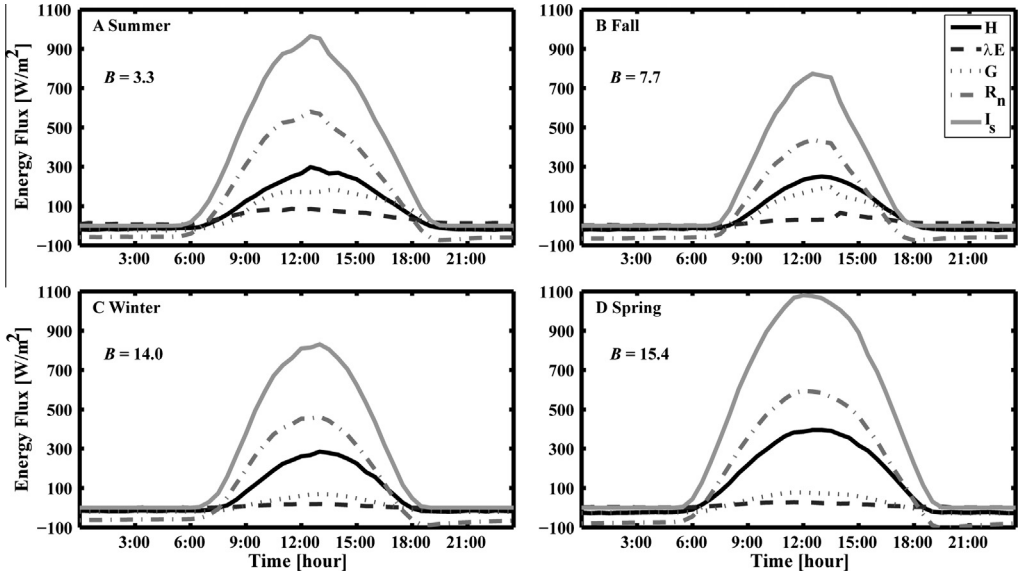

Fig. 6. Seasonally-averaged diurnal variation (in local time) of energy fluxes over the study period. I_s is incoming solar radiation, R_n is net radiation, H is sensible heat flux, λE is latent heat flux and G is ground heat flux. A. Summer (July 1 to September 30). B. Fall (October 1 to December 31). C. Winter (January 1 to March 31). D. Spring (April 1 to June 30). The mid-day Bowen ratio (B) estimated for each season is shown.

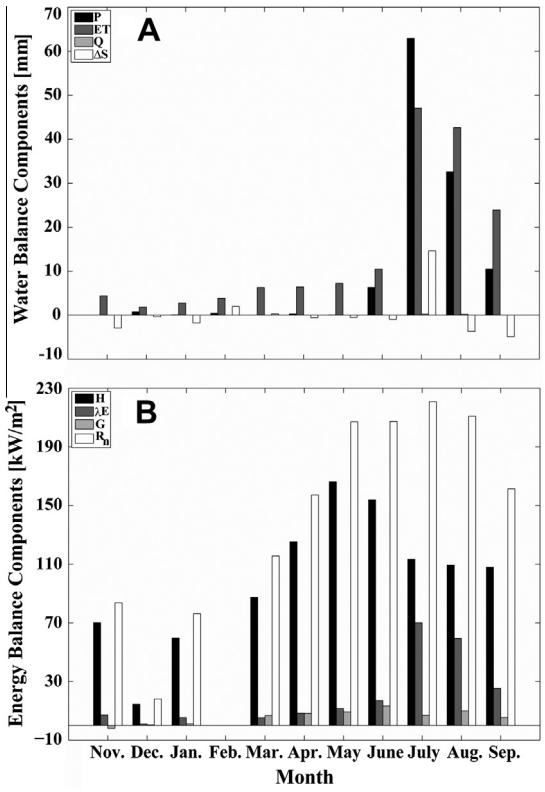

Fig. 8. A. Monthly water balance components (mm): precipitation (P), evapotranspiration (ET), runoff (Q) and change in soil water storage (ΔS). B. Monthly energy balance components (kW/m^2): sensible heat flux (H), latent heat flux (λE), ground heat flux (G) and net radiation (R_n). A and B are shown from November 2010 to September 2011 with a data gap in February for B.

P for the rain gauge type used (Scott, 2010), but likely closer to 10% for the high wind speeds at JER, (2) the unavoidable mismatch between the fixed watershed area and the time-variable EC footprint, and (3) the slow extraction of stored soil water by transpiration from caliche layers below 30 cm or from deeper subsurface storages filled through periodic recharge events in the hillslopes and by channel transmission losses. The latter explanation is based on the observation that ET occurs at greater rates than negative changes in soil moisture (ΔS) from the upper 30 cm during the fall, winter and spring seasons (Table 3). Interestingly, high P during July leads to an increase in both ΔS and ET, as available water is sufficient to exceed evapotranspiration demand (as in Mahmood and Vivoni, 2011). Vegetation greening over the months of August and September leads to sustained ET levels that consume both P and stored soil water (negative ΔS). Overall, runoff at the outlet (Q) is a small fraction of precipitation (0.39% of P) and occurs exclusively during the summer. Monthly errors (e) in the water balance (Table 3) were relatively large (−45 mm over the period or 39% of P) and negative, with values exceeding the analysis of Scott (2010). A portion of these errors can be attributed to missing observations (marked by a * in Table 3), while another portion is due to the inherent difficulty in closing the monthly water balance using independent and spatially-distributed sensors, each characterized by measurement uncertainty as well as issues of representativeness of the basin-averaged conditions, in particular for ET.

The energy balance components in Fig. 8b follow a monthly progression consistent with an increase in radiation and water availability from the winter to the summer seasons. Note that data gaps in December lead to lower than expected energy fluxes. Interestingly, the timing of the peak monthly flux in each energy component varies considerably: R_n in July, H in May, λE in July and G in June. R_n peaks in July due to the higher difference between net shortwave and longwave radiation, $R_n = SW + LW = (SW_{in} - SW_{out}) + (LW_{in} - LW_{out})$, as shown in Table 3, as LW increases due to surface cooling in wetter soils and a moister and warmer atmosphere. Clearly, the decrease in LW (related to lower soil temperatures) plays a larger role in the increase in R_n than the decrease in albedo from vegetation greening (linked to SW) at the onset of the NAM. Sensible heat flux (H) peaks in May and is reduced in response to a storm event in June, which increases both λE and G, the latter due to a higher thermal conductivity of wetter soils (e.g., Schelde et al., 1998). At the monthly scale, H ranges from 51% to 84% of R_n with an average of 69% over the period, while λE consists of 5% to 32% of R_n and averages to 14%. Ground heat flux consistently has a low contribution, but exceeds λE during the dry month of March. Monthly G accounts for day- and night-time contributions leading to the low overall values. Table 3 also presents the monthly errors in the energy balance (ε), referred to as the closure error (Twine et al., 2000), ranging from 2 to 32 kW/m^2 or 10% to 15% of monthly R_n. Closure errors of this magnitude are common when using the eddy covariance method but it is still unknown if this leads to real underestimations of turbulent heat fluxes (e.g., Dugas et al., 1996; Nie et al., 1992; Mahrt, 1998; Twine et al., 2000; Scott, 2010). A portion of these errors can be attributed to missing observations (marked by a * in Table 3), while another portion is due to the difficulty in closing the monthly energy balance within the EC footprint where a spatial mismatch exists between R_n and G measurements with those of the turbulent fluxes (H and λE).

3.3. Spatiotemporal analysis for individual summer storm events

The high-resolution observations allow analyses of the watershed dynamics for individual storm periods. We selected four consecutive periods (July 7, July 20, July 23 and August 9, 2011) that spanned the seasonal progression of the NAM and had outlet runoff of comparable duration and timing during the day (Templeton, 2011). Fig. 9 presents the variability in channel runoff at the four flumes for each event along with the rainfall observations lasting one to two hours in the early afternoon. A comparison across the flumes provides an indication of the sub-watershed runoff and channel transmission losses (Goodrich et al., 1997; Newman et al. (2006b)). For example, the increasing runoff volume and a delay in the peak runoff between Flumes 3 and 2 (Fig. 3d) indicates that runoff is transported downstream with minimal channel losses. This is consistent with the caliche-lined channel bottoms present in the upper parts of the watershed. In contrast, the outlet flume produces runoff earlier than the upper flume sites and often of a lower volume. This is explained by: (1) the coarse channel sands and gravels near the outlet which lead to transmission losses of the runoff measured at upstream flumes, and (2) the presence of a large tributary near the outlet, measured by Flume 1, which leads to a quicker runoff response of a more local origin. Clearly, spatial variability is present in the runoff generation and routing within the watershed. Over the four events, the runoff ratio (Q/P) varied from <1% to 2.4% among the flumes (Templeton, 2011), depending on the rainfall intensity, the antecedent wetness set by the length of the preceding interstorm period and the sub-watershed and channel properties. These results are slightly lower than Turnbull et al. (2013) whose rainfall–runoff analysis at the watershed outlet showed that the most probable Q/P during 2003–2011 was ~6%. However, the wide distributions in Q and P found by Turnbull et al. (2013) suggest that the Q/P values at the individual flumes during the four events are reasonably estimated.

The spatiotemporal variability of the watershed response can also be inspected in the soil moisture data during post-storm periods lasting a few days after each event, as shown in Fig. 10. We ob-

Table 3
Spatially-averaged monthly water balance components (mm) and its monthly error (e) computed as $e = P - ET - Q - \Delta S$ and monthly radiation and energy balance components (kW/m^2) and the monthly energy balance error (ε) computed as $\varepsilon = R_n - H - \lambda E - G$. Some data is missing in months marked with * and February (–) was not included due to equipment failure. The total column indicates the total (mm or kW/m^2) over the available months.

	Year and month											
	2010		2011									
Component	November	December*	January*	February	March*	April*	May	June	July	August	September	Total
P (mm)	0	0.74	0.09	0.43	0	0.27	0.04	6.32	62.93	32.57	10.49	113.88
Q (mm)	0	0	0	0	0	0	0	0	0.24	0.20	0	0.44
ET (mm)	4.38	1.87	2.77	3.84	6.29	6.41	7.23	10.46	47.09	42.64	23.91	156.89
ΔS (mm)	−2.90	−0.36	−1.77	1.98	0.27	−0.55	−0.5	−0.95	14.63	−3.70	−4.89	1.26
e (mm)	−1.48	−0.77	−0.91	−5.39	−6.56	−5.60	−6.69	−3.19	0.97	−6.57	−8.53	−44.72
I_s (kW/m^2)	279	65	246	–	303	400	527	535	477	447	392	3671
R_n (kW/m^2)	84	18	76	–	116	157	207	207	221	211	161	1458
SW (kW/m^2)	207	48	183	–	223	292	380	393	354	340	293	2713
LW (kW/m^2)	−123	−30	−107	–	−107	−134	−173	−185	−133	−129	−131	−1252
H (kW/m^2)	70	15	60	–	87	125	166	154	113	109	108	1007
λE (kW/m^2)	7	1	5	–	5	8	12	17	70	59	25	209
G (kW/m^2)	−2	0	1	–	7	8	9	13	7	10	5	58
ε (kW/m^2)	10	2	12	–	17	17	22	25	31	32	23	191

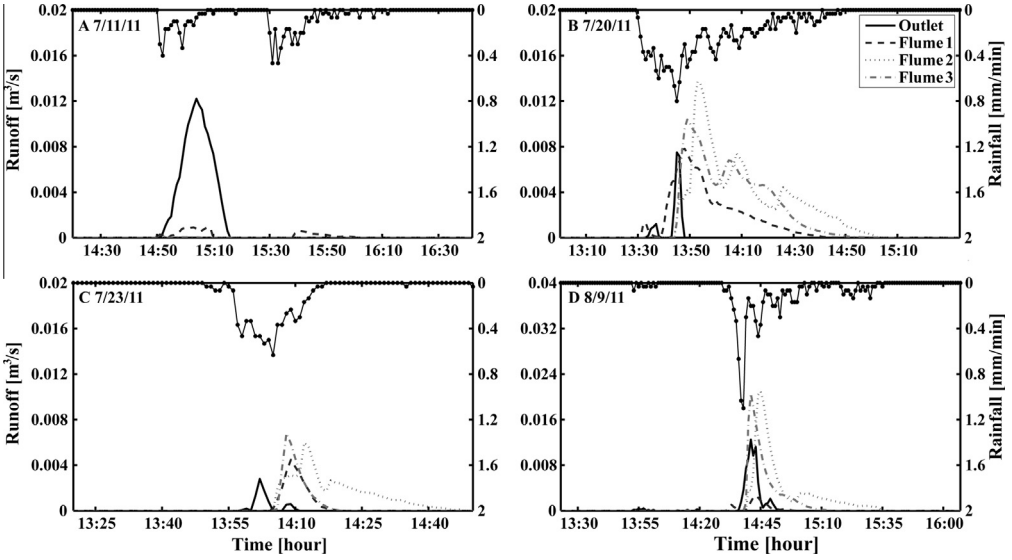

Fig. 9. Rainfall (mm/min) and channel runoff (m^3/s) at the four flumes at 1 min intervals for four periods. A. July 11, 2011. B. July 20, 2011. C. July 23, 2011. D. August 9, 2011.

tained average conditions at 30 min intervals for all sites in each transect: T1 (north-facing), T2 (south-facing) and T3 (west-facing) at 5 cm and integrated over 40 cm depths (labeled as Profile). As expected, soil moisture varies more considerably after the storms at the shallower depths as compared to the entire profile (i.e., more rapid rises and steeper recessions). Some of the moisture losses from the shallower soil lead to gains over the profile, indicating that vertical redistribution is present at the transect sites. Pre-storm moisture levels in the upper soil are reached in two to three days after a storm in the absence of subsequent rainfall, consistent with Kurc and Small (2004) and Gutiérrez-Jurado et al. (2007) for other sites in the Chihuahuan Desert, while the entire profile returns to pre-storm levels within approximately 2 weeks. Interestingly, the surface and profile soil moisture values were lowest for the north-facing T1 throughout the post-storm periods, as corroborated in Fig. 11. Here, shallow soil moisture values at all transect sites were averaged in time over 18 events defined for rainfall amounts greater than 1 mm (over a time window from 30 min prior to 24 h after each rainfall). The lower soil moisture at T1 and its internal differences within the transect are likely due to variations in soil properties that are distinguishable from soil color changes in the UAV-based imagery. There does not seem to be a strong control of aspect on soil moisture conditions during storms. Instead, downslope sites near the channel network appear to be wetter in T2 and T3, suggesting lateral soil moisture redistribution associated with runoff generation during storm events. In addition, spatial variations in soil moisture occur over distances in the transects on the order of 10 m, based on the average spacing between the sensor locations along each transect (Fig. 3a).

Fig. 12 presents the energy balance components after the four storm periods lasting until the next event exceeding 1 mm in rainfall. Net radiation is primarily affected by daily variations in cloud cover and differences in soil temperature after wetting periods. Sensible heat flux is depressed following a rainfall event and takes several days or up to a week to reach pre-storm levels as soil temperatures increase during drying. In contrast, latent heat fluxes are maximized in the first day following a storm and slowly decrease during interstorm periods as the surface and profile soil layers dry (Fig. 10). Since interstorm periods typically last less than 2 weeks, frequent changes in the dominance of sensible or latent heat fluxes occur during the NAM. Ground heat flux, on the other hand, exhibits limited sensitivity to the sequence of storm and interstorm periods, with a slight decrease observed for 24 h after a rain event. The variable rates at which energy components return

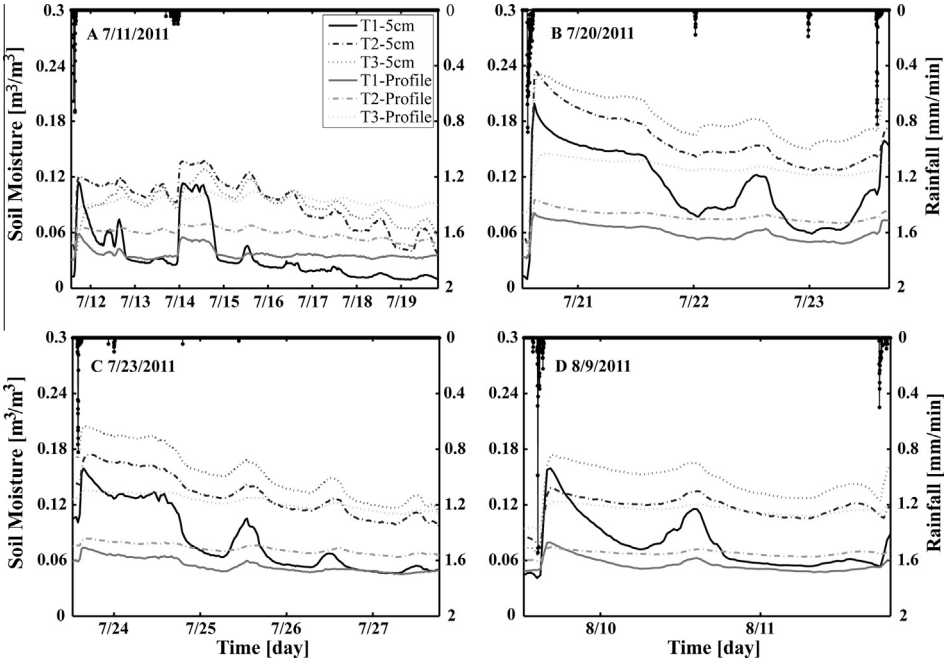

Fig. 10. Soil moisture (m^3/m^3) averaged over transect locations at 5 cm and 40 cm profiles at 30 min intervals for four periods. A. July 11, 2011. B. July 20, 2011. C. July 23, 2011. D. August 9, 2011.

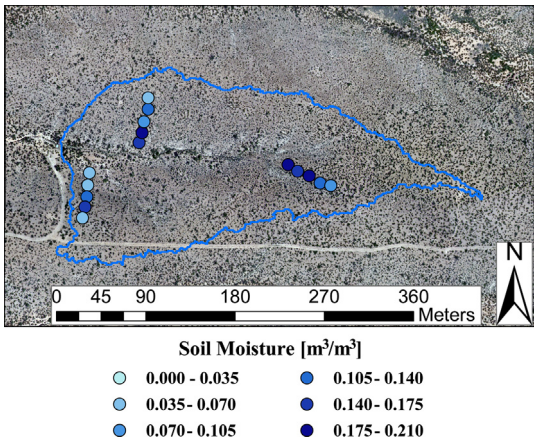

Fig. 11. Spatial distribution of soil moisture (m^3/m^3) at 5 cm depth averaged over storm periods.

to normalcy following a storm illustrate the importance of high-resolution temporal sampling in the semiarid watershed. While the variations in energy fluxes are clearly linked to land surface conditions, it remains unclear how spatial patterns in soil moisture and temperature affect the components in the heterogeneous landscape as there is a mismatch between the various measurement scales, as discussed in Vivoni et al. (2010b).

3.4. Value of high-resolution observations for evapotranspiration estimation

The high-resolution observations allow estimating *ET* through a number of alternative approaches in the semiarid watershed. Fig. 13 presents monthly *ET* over the period September 2010 to September 2011 obtained as a water balance residual using single site (ET_{single}) and distributed (ET_{basin}) soil moisture measurements to estimate *P* and ΔS, along with the eddy covariance estimates (ET_{EC}) used as a ground-truth. Over the period analyzed, ET_{basin} was closer in magnitude to ET_{EC} than ET_{single} for all months, except August 2011. During the NAM onset in July, the improvement when using ET_{basin} is considerable, due to capturing more representative soil moisture changes in the basin as compared to the single site at the tower. Table 4 compares the two approaches in terms of the daily mean absolute error (MAE) between the *ET* estimate and ET_{EC}. These comparisons indicate that including the spatial variability in precipitation and soil water storage changes enhances the use of the water balance residual approach to estimate *ET* relative to the eddy covariance method. Moreover, it confirms the assertion by Scott (2010) that a portion of the errors in using the watershed water balance to estimate *ET* are due to the spatial mismatch between ET_{EC} and ET_{single}. If *P* and ΔS are sampled in a distributed fashion, a large and consistent improvement (~40% reduction in error) can be achieved in estimating evapotranspiration from the water balance residual in the semiarid watershed.

Fig. 14 compares the daily relation between evapotranspiration and depth-averaged soil moisture using the distributed and single site measurements of θ (circles) and the piecewise linear relations (solid lines) estimated using an objective, nonlinear optimization method, as in Vivoni et al. (2008a). The regression lines are characterized by the parameters of the *ET*-θ relation shown in Table 4. Differences in the lower and upper range of soil moisture values are due to variations in the sensor type (Hydra Probe at distributed locations and CS616 at the single tower site) that do not affect the overall analysis. Clearly, the distributed measurements lead to a piecewise linear relation that exhibits a plateau in *ET*, with ET_{max} of similar magnitudes in both approaches. The missing plateau in the single site relation implies that an adequate representation of soil moisture controls on *ET* is not captured, likely due to the mismatch between the site measurement and the EC footprint (Vivoni et al., 2010b). The distributed measurements, on the other hand, are able to depict that wet soil conditions distributed throughout the semiarid watershed are linked to ET_{max}. Once derived, the piecewise linear regressions also serve as estimation method for daily *ET* based on single site or distributed measurements, as performed in many hydrologic models. Table 4 reports the MAE between ET_{EC} and estimates from ET_{single} and ET_{basin} using the piece-

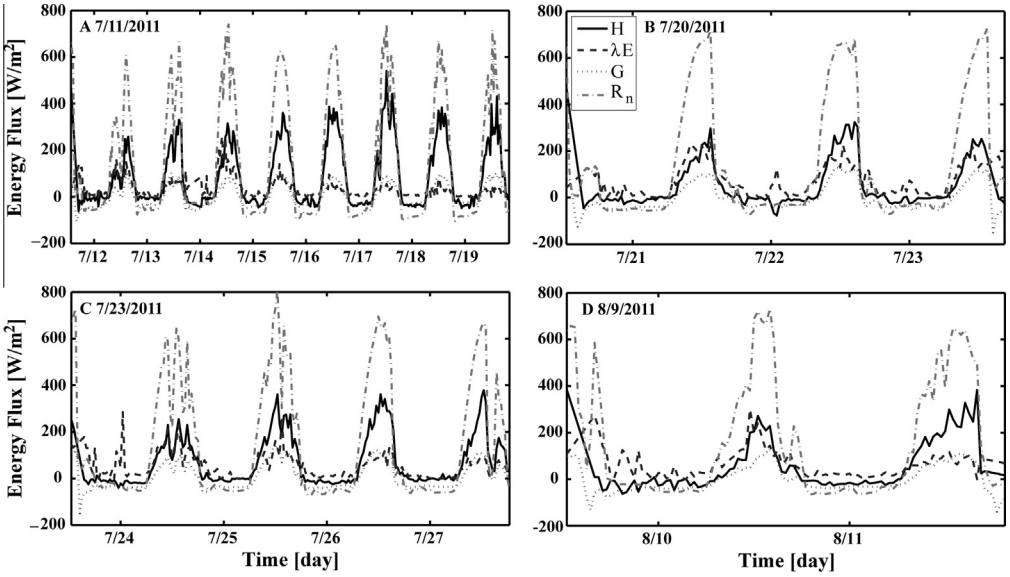

Fig. 12. Energy balance components (W/m^2) at 30 min intervals for four periods. A. July 11, 2011. B. July 20, 2011. C. July 23, 2011. D. August 9, 2011.

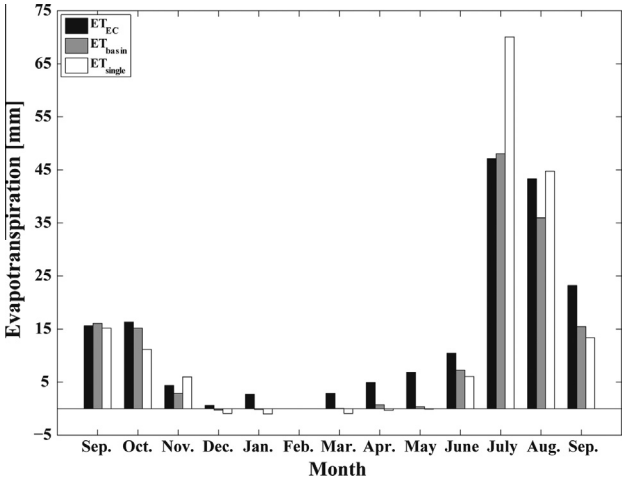

Fig. 13. Monthly evapotranspiration (September 2010–2011) from the eddy covariance method (ET_{EC}) and the water balance residual using the spatially-averaged soil moisture and precipitation data (ET_{basin}) or soil moisture and precipitation measurements at the tower (ET_{single}). Spatial averaging of soil moisture and precipitation data was performed as in Fig. 5.

Table 4
Comparison of single (ET_{single}) and distributed (ET_{basin}) approaches for estimating *ET* using the water balance residual and the daily relation between *ET* and θ. MAE is the mean absolute error in *ET* between the estimate and the EC observation (ET_{EC}). Parameters of the piecewise linear relation of *ET* and θ are shown for each approach.

	Single measurement	Distributed measurement
Water balance residual		
MAE [mm/day]	0.234	0.133
Piecewise linear regression		
MAE (mm/day)	0.252	0.235
Regression parameters		
E_w (mm/day)	0.174	0.283
ET_{max} (mm/day)	2.75	2.70
θ_h (m^3/m^3)	0.0001	0.0001
θ_w (m^3/m^3)	0.03	0.0005
θ^* (m^3/m^3)	0.18	0.10
ϕ (m^3/m^3)	0.18	0.14

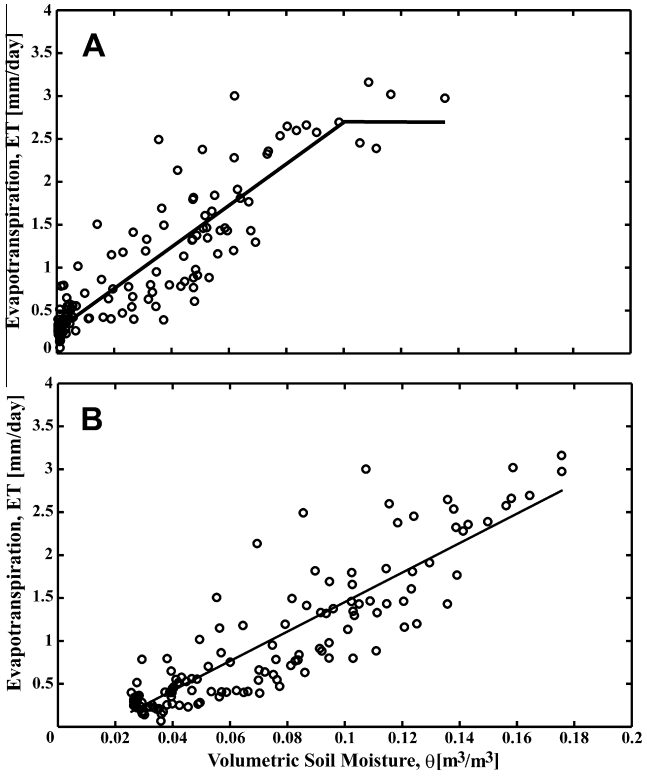

Fig. 14. Daily relation between *ET* (mm/day) and θ (m^3/m^3) with data (circles) and piecewise linear regressions (solid lines) for all available days with coincident datasets. Distributed (A) and single (B) measurements of θ.

wise linear relation as a measure of goodness of fit. For estimating the MAE, all values in the *ET*-θ relation are retained, including times of negligible soil moisture and evapotranspiration, to ensure that the entire range of variability is sampled. The distributed measurements lead to an improvement in estimating *ET* (~7% reduction in error) as compared to the single site data. The smaller improvements and the higher magnitudes of MAE as compared to the water balance residual approach are due to the reduction in variability caused by fitting the piecewise linear relation to the

data. Nevertheless, an established *ET*-θ relation using distributed measurements has a comparable accuracy to the single site, water balance residual approach.

4. Summary and conclusions

In this study, we used high-resolution observations in a mixed shrubland watershed of the Jornada Experimental Range in southern New Mexico to characterize the temporal dynamics of water and energy fluxes at the seasonal, monthly and storm event scales and provide insight into their spatial distributions and linkages. Understanding seasonal variations of atmospheric, hydrologic and ecologic processes in arid and semiarid watersheds of the NAM region has garnered increased attention in the last decade (e.g., Leung et al., 2003; Scott et al., 2004; Gochis et al., 2006; Watts et al., 2007; Kurc and Small, 2007; Notaro et al., 2010; Vivoni, 2012b). More recently, the hydrologic connectivity of a landscape has been hypothesized as contributing to downstream vegetation conditions, in particular where mosaics of bare soils, herbaceous plants and woody shrubs and trees coexist (e.g., Ludwig et al., 2005; Peters et al., 2010; Bestelmeyer et al., 2011). Through the novel application of an environment sensor network and UAV-based imagery products, this work provides a first look at the importance of the spatial distribution of landscape conditions on the water and energy fluxes in the semiarid watershed. Application of the UAV products contributed significantly to characterizing elevation, aspect and upstream area distributions used to interpolate site data and to interpret the spatial patterns of hydrologic response (see Rango and Vivoni, 2012, for a discussion of the improvements of terrain and hydrologic features offered by UAV imagery relative to traditional data sources). Consistent with Duniway et al. (2010), we found that soil moisture is redistributed from upper layers to the caliche horizon during storms, potentially serving as a moisture source to vegetation during drier months. We also discovered a downslope redistribution of soil water along the hillslopes, with sites closer to the main channel exhibiting higher wetness, though local soil variations also play a role. Spatial variations in soil moisture were likely important in leading to differential runoff production among the hillslopes and within the sub-watersheds. Channel runoff data showed that upper reaches with caliche-lined bottoms moved flood pulses downstream efficiently, while the lower reaches experienced significant channel transmission losses.

The distributed soil moisture measurements were also used to show that *ET* is linked to the spatially-averaged conditions within the heterogeneous watershed. During most of the year, *ET* is a relatively small fraction of the energy balance, with the Bowen ratio varying from $B = 14$ (winter) to 3.3 (summer). Nevertheless, *ET* is the major water loss in the watershed with high rates of evapotranspiration after storm events and lower rates of plant transpiration from deeper soil water during dry months. During interstorm periods, latent and sensible heat flux return to pre-storm levels within a few days as surface and profile soil moisture is consumed. Seasonal shifts in the energy and water balance due to summer water availability are also accompanied by vegetation greening during the NAM, as measured through a decrease in surface albedo. A result of the spatiotemporal dynamics is a heterogeneous watershed condition that needs to be sampled in a distributed manner and that measurements of precipitation and soil moisture at a single site are inadequate. We found that the water balance approach for estimating monthly *ET* was improved significantly (on average a ~40% reduction in error, with better performance during particular months, Fig. 13) when accounting for the spatial distribution in soil water storage changes in the watershed as compared to measurements at the EC tower slightly outside the basin. Similarly, the daily *ET*-θ relation derived from spatially-distributed data exhibited a more reasonable form and yielded better predictions relative to the EC measurements (on average, a ~7% reduction in error, Table 4). Clearly, the use of distributed measurements of precipitation and soil moisture were more appropriate for estimating *ET* losses. In this study, the most critical improvement was obtained from distributed measurements of soil water storage and its changes in time since these accounted for the spatial distribution in the basin of factors affecting it, specifically terrain position, soil variations and vegetation patterns.

Overall, the combined use of an environmental sensor network and UAV-based imagery provides a new means for studying hydrologic processes in semiarid watersheds exhibiting a high degree of spatial heterogeneity and seasonal evolution in land surface characteristics. For the purposes of estimating *ET* at the watershed scale, a network of distributed precipitation and soil moisture sensors along with channel runoff measurements can yield accurate results at the monthly scale using the water balance residual method or at the daily scale after establishing an *ET*-θ relation using EC observations. A promising method could be to identify a monitoring site that represents well the spatially-averaged conditions in the basin based on the existing network (e.g., Vachaud et al., 1985; Vivoni et al., 2008b) and utilize this to obtain *ET* estimates from the various methods outlined here. The high-resolution observations also have the potential to serve as a dataset for the application of distributed hydrologic models (Ivanov et al., 2004; 2008) that can provide a means to: (1) explore the underlying hydrologic mechanisms at different time scales, (2) extrapolate conditions in space and time, and (3) test how hydrologic connectivity affects downstream soil water availability and vegetation states. For example, Vivoni (2012a) discusses how the integrated use of spatial observations and modeling can yield benefits for characterizing the spatial patterns and processes in semiarid watersheds. In addition, the virtual laboratories provided by spatially-explicit watershed models confirmed with spatial data can provide a window into understanding the causes and consequences of desertification processes that have characterized arid and semiarid watersheds in the NAM region in the last century.

Acknowledgements

We thank Craig Tweedie, Aline Jaimes amd Gesuri Ramirez from the University of Texas at El Paso for help with implementing a telemetry network at the site. We are also grateful for help from John Anderson and staff members at the Jornada Experimental Range. We thank funding from the U.S. Army Research Office (Grant 56059-EV-PCS) and the Jornada Long-Term Ecological Research project (National Science Foundation Grant DEB-1235828). We acknowledge two reviewers whose comments helped improve the original manuscript.

References

Abrahams, A.D., Parsons, A.J., Wainwright, J., 2003. Disposition of rainwater under creosotebush. Hydrol. Process. 17, 2555–2566.

Barnsley, M.J., Hobson, P.D., Hyman, A.H., Lucht, W., Muller, J.-P., Strahler, A.H., 2000. Characterizing the spatial variability of broadband albedo in a semidesert environment for MODIS validation. Rem. Sens. Environ. 74, 58–68. http://dx.doi.org/10.1016/S0034-4257(00)00123-1.

Bestelmeyer, B.T., Goolsby, D.P., Archer, S.R., 2011. Spatial perspectives in state-and-transition models: a missing link to land management? J. Appl. Ecol. 48, 746–757. http://dx.doi.org/10.1111/j.1365-2664.2011.01982.x.

Breshears, D.D., Nyhan, J.W., Heil, C.E., Wilcox, B.P., 1998. Effects of woody plants on microclimate in a semiarid woodland: soil temperature and evaporation in canopy and intercanopy patches. Int. J. Plant Sci. 159, 1010–1017. http://dx.doi.org/10.1086/314083.

Browning, D.M., Laliberte, A.S., Rango, A., Herrick, J.E., 2009. Prospects for phenological monitoring in an arid southwestern U.S. rangeland using field observations with hyperspatial and moderate resolution imagery. In: American Geophysical Union Fall meeting, San Francisco, California.

Browning, D.M., Duniway, M.C., Laliberte, A.S., Rango, A., 2012. Hierarchical analysis of vegetation dynamics over 71 years: soil-rainfall interactions in a Chihuahuan Desert ecosystem. Ecol. Appl. 22, 909–926.
Campbell, J.E., 1990. Dielectric properties and influence of conductivity in soils at one to fifty Megahertz. Soil Sci. Soc. Am. J. 54, 332–341.
Canfield, R.H., 1941. Application of the line interception method in sampling range vegetation. J. For. 39, 388–394.
Cavanaugh, M.L., Kurc, S.A., Scott, R.L., 2011. Evapotranspiration partitioning in semiarid shrubland ecosystems: a two-site evaluation of soil moisture control on transpiration. Ecohydrology 4, 671–681. http://dx.doi.org/10.1002/eco.157.
Chen, F., Mitchell, K., Schaake, J., Xue, Y., Pan, H.-L., Koren, V., Duan, Q.Y., Ek, M., Betts, A., 1996. Modeling of land surface evaporation by four schemes and comparisons with FIFE observations. J. Geophys. Res. 101, 7251–7268. http://dx.doi.org/10.1029/95JD02165.
Douglas, M.W., Maddox, R.A., Howard, K., Reyes, S., 1993. The Mexican monsoon. J. Climate 6, 1665–1677. http://dx.doi.org/10.1175/1520-0442(1993) 006<1665:TMM>2.0.CO;2.
Dugas, W.A., Hicks, R.A., Gibbens, R.P., 1996. Structure and function of C3 and C4 Chihuahuan Desert plant communities. Energy balance components. J. Arid Environ. 34, 63–79. http://dx.doi.org/10.1006/jare.1996.0093.
Duniway, M.C., Snyder, K.A., Herrick, J.E., 2010. Spatial and temporal patterns of water availability in a grass-shrub ecotone and implications for grassland recovery in arid environments. Ecohydrology 3, 55–67. http://dx.doi.org/10.1002/eco.94.
Foken, T., 2006. 50 Years of the Monin–Obukhov similarity theory. Bound. Lay. Meteorol. 119, 431–447. http://dx.doi.org/10.1007/s10546-006-9048-6.
Forzieri, G., Castelli, F., Vivoni, E.R., 2011. Vegetation dynamics within the North American monsoon region. J. Climate 24, 1763–1783. http://dx.doi.org/10.1175/2010JCLI3847.1.
Gebremichael, M., Vivoni, E.R., Watts, C.J., Rodriguez, J.C., 2007. Submesoscale spatiotemporal variability of North American monsoon rainfall over complex terrain. J. Climate 20, 1751–1773. http://dx.doi.org/10.1175/JCL14093.1.
Gibbens, R.P., McNeely, R.P., Havstad, K.M., Beck, R.F., Nolen, B., 2005. Vegetation changes in the Jornada basin from 1858 to 1998. J. Arid Environ. 61, 651–668. http://dx.doi.org/10.1016/j.jaridenv.2004.10.001.
Gill, P.E., Murray, W., Wright, M.H., 1981. Practical Optimization. Academic Press, London, UK, pp. 402.
Gochis, D.J., Brito-Castillo, L., Shuttleworth, W.J., 2006. Hydroclimatology of the North American monsoon region in northwest Mexico. J. Hydrol. 316, 53–70. http://dx.doi.org/10.1016/j.jhydrol.2005.04.021.
Goodrich, D.C., Lane, L.J., Shillito, R.M., Miller, S.N., Syed, K.H., Woolhiser, D.A., 1997. Linearity of basin response as a function of scale in a semiarid watershed. Water Resour. Res. 33, 2951–2965. http://dx.doi.org/10.1029/97WR01422.
Goodrich, D.C., Unkrich, C.L., Keefer, T.O., Nichols, M.H., Stone, J.J., Levick, L.R., Scott, R.L., 2008. Event to multidecadal persistence in rainfall and runoff in southeast Arizona. Water Resour. Res. 44, W05S14. http://dx.doi.org/10.1029/2007WR00622.
Gutiérrez-Jurado, H.A., Vivoni, E.R., Harrison, J.B.J., Guan, H., 2006. Ecohydrology of root zone water fluxes and soil development in complex semiarid rangelands. Hydrol. Process. 20 (15), 3289–3316. http://dx.doi.org/10.1002/hyp.6333.
Gutiérrez-Jurado, H.A., Vivoni, E.R., Istanbulluoglu, E., Bras, R.L., 2007. Ecohydrological response to a geomorphically significant flood event in a semiarid catchment with contrasting ecosystems. Geophys. Res. Lett. 34, L24S25. http://dx.doi.org/10.1029/2007GL030994.
Hargreaves, G.H., Samani, Z.A., 1982. Estimating potential evapotranspiration. J. Irrig. Drain. Eng. 108, 223–230.
Hargreaves, G.H., Samani, Z.A., 1985. Reference crop evapotranspiration from temperature. Trans. ASAE 1, 96–99.
Herrick, J.E., Van Zee, J.W., Havstad, K.M., Burkett, L.M., Whitford, W.G., 2009. Monitoring Manual for Grassland, Shrubland and Savanna Ecosystems. University of Arizona Press, Tucson, AZ, pp. 44.
Huxman, T.E., Wilcox, B.P., Breshears, D.D., Scott, R.L., Snyder, K.A., Small, E.E., Hultine, K., Pockman, W.T., Jackson, R.B., 2005. Ecohydrological implications of woody plant encroachment. Ecology 86, 308–319. http://dx.doi.org/10.1890/03-0583.
ISO 4359, 1983. Liquid Flow Measurement in Open Channels – Rectangular, Trapezoidal, and U-Shaped Flumes. International Organization of Standards, Geneva, Switzerland.
Ivanov, V.Y., Vivoni, E.R., Bras, R.L., Entekhabi, D., 2004. Catchment hydrologic response with a fully-distributed triangulated irregular network model. Water Resour. Res. 40, W11102. http://dx.doi.org/10.1029/2004WR003218.
Ivanov, V.Y., Bras, R.L., Vivoni, E.R., 2008. Vegetation-hydrology dynamics in complex terrain of semiarid areas. I. A mechanistic approach to modeling dynamic feedbacks. Water Resour. Res. 44, W03429. http://dx.doi.org/10.1029/2006WR005588.
Kormann, R., Meixner, F.X., 2001. An analytical footprint model for non-neutral stratification. Bound. Lay. Meteorol. 99, 207–224. http://dx.doi.org/10.1023/A:1018991015119.
Kurc, S., Small, E.E., 2004. Dynamics of evapotranspiration in a semiarid grassland and shrubland ecosystems during the summer-monsoon season, central New Mexico. Water Resour. Res. 40, W09305. http://dx.doi.org/10.1029/2004WR003068.
Kurc, S.A., Small, E.E., 2007. Soil moisture variations and ecosystem-scale fluxes of water and carbon in semiarid grassland and shrubland. Water Resour. Res. 43, W06416. http://dx.doi.org/10.1029/2006WR005011.
Laliberte, A.S., Rango, A., 2011. Image processing and classification procedures for analysis of sub-decimeter imagery acquired with an unmanned aircraft over arid rangelands. GISci. Rem. Sens. 48, 4–23. http://dx.doi.org/10.2747/1548-1603.48.1.4.
Laliberte, A.S., Winters, C., Rango, A., 2008. A procedure for orthorectification of sub-decimeter resolution imagery obtained with an unmanned aerial vehicle (UAV). In: ASPRS Annual Conference Proceedings, Portland, OR.
Laliberte, A.S., Browning, D.M., Rango, A., 2012. A comparison of three feature selection methods for object-based classification of sub-decimeter resolution UltraCam-L imagery. Int. J. Appl. Earth Observ. Geoinform. 15, 70–78. http://dx.doi.org/10.1016/j.jag.2011.05.011.
Larson, L.W., Peck, E.L., 1974. Accuracy of precipitation measurements for hydrologic modeling. Water Resour. Res. 10, 857–863.
Lawrence, J.E., Hornberger, G.M., 2007. Soil moisture variability across climate zones. Geophys. Res. Lett. 34, L20402. http://dx.doi.org/10.1029/2007GL031382.
Leung, L.R., Qian, Y., Bian, X.D., 2003. Hydroclimate of the western United States based on observations and regional climate simulation of 1981–2000. Part 1: seasonal statistics. J. Climate 16, 1892–1911. http://dx.doi.org/10.1175/1520-0442(2003) 016<1892:HOTWUS>2.0.CO;2.
Ludwig, J.A., Wilcox, B.P., Breshears, D.D., Tongway, D.J., Imeson, A.C., 2005. Vegetation patches and runoff-erosion as interacting ecohydrological processes in semiarid landscapes. Ecology 86, 288–297. http://dx.doi.org/10.1890/03-0569.
Mahmood, T.H., Vivoni, E.R., 2011. A climate-induced threshold in hydrologic response in a semiarid ponderosa pine hillslope. Water Resour. Res. 47, W09529. http://dx.doi.org/10.1029/2011WR010384.
Mahrt, L., 1998. Flux sampling errors for aircraft and towers. J. Atmos. Ocean. Technol. 15, 416–429. http://dx.doi.org/10.1175/1520-0426(1998)015<0416:FSEFAA>2.0.CO;2.
Monger, H.C., 2006. Soil development in the Jornada Basin. In: Havstad, K.M., Huenneke, L.F., Schlesigner, W.H. (Eds.), Structure and Function of a Chihuahuan Desert Ecosystem. Oxford University Press, New York, NY, pp. 81–106.
Monger, H.C., Bestelmeyer, B.T., 2006. The soil-geomorphic template and biotic change in arid and semi-arid ecosystems. J. Arid Environ. 65, 207–218. http://dx.doi.org/10.1016/j.jaridenv.2005.08.012.
Mueller, E.N., Wainwright, J., Parsons, A.J., 2007. Impact of connectivity on the modeling of overland flow within semiarid shrubland environments. Water Resour. Res. 43, W09412. http://dx.doi.org/10.1029/2006WR005006.
Newman, B.D., Wilcox, B.P., Archer, S., Breshears, D.D., Dahm, C.N., Duffy, C.J., McDowell, N.G., Phillips, F.M., Scanlon, B.R., Vivoni, E.R., 2006a. The ecohydrology of arid and semiarid environments: a scientific vision. Water Resour. Res. 42, W06302. http://dx.doi.org/10.1029/2005WR004141.
Newman, B.D., Vivoni, E.R., Groffman, A.R., 2006b. Surface water-groundwater interactions in semiarid drainages of the American Southwest. Hydrol. Process. 20, 3371–3394. http://dx.doi.org/10.1002/hyp.6336.
Nie, D., Kanemasu, E.T., Fritschen, L.J., Weaver, H.L., Smith, E.A., Verma, S.B., Field, R.T., Kustas, W.P., Stewart, J.B., 1992. An intercomparison of surface energy flux measurement systems used during FIFE 1987. J. Geophys. Res. 97, 18715–18724.
Notaro, M., Liu, Z.Y., Gallinore, R.G., Williams, J.W., Gutzler, D.S., Collins, S., 2010. Complex seasonal cycle of ecohydrology in the Southwest United States. J. Geophys. Res. Biogeosci. 115, G04034. http://dx.doi.org/10.1029/2010JG001382.
Okin, G.S., Parsons, A.J., Wainwright, J., Herrick, J.E., Bestelmeyer, B.T., Peters, D.C., Fredericksen, E.L., 2009. Do changes in connectivity explain desertification? Bioscience 59, 237–244. http://dx.doi.org/10.1525/bio.2009.59.3.8.
Peters, D.P.C., Herrick, J.E., Monger, H.C., Huang, H., 2010. Soil-vegetation-climate interactions in arid landscapes: effects of the North American monsoon on grass recruitment. J. Arid Environ. 74, 618–623. http://dx.doi.org/10.1016/j.jaridenv.2009.09.015.
Pierson, F.B., Blackburn, W.H., Vanvactor, S.S., Wood, J.C., 1994. Partitioning small-scale spatial variability of runoff and erosion on sagebrush rangeland. Water Resour. Bullet. 30, 1081–1089.
Potts, D.L., Scott, R.L., Bayram, S., Carbonara, J., 2010. Woody plants modulate the temporal dynamics of soil moisture in a semi-arid mesquite savanna. Ecohydrology 3, 20–27. http://dx.doi.org/10.1002/eco.91.
Rango, A., Vivoni, E.R., 2012. Hydrology with Unmanned Aerial Vehicles (UAVs). In: AGU Chapman Conference on Remote Sensing of the Terrestrial Water Cycle. Kona, Hawaii.
Rodríguez-Iturbe, I., Porporato, A., 2004. Ecohydrology of Water-Controlled Ecosystems. Cambridge University Press, Cambridge, UK, pp. 464.
Salinas-Zavala, C.A., Douglas, A.V., Díaz, H.F., 2002. Interannual variability of NDVI in northwest Mexico: associated climatic mechanisms and ecological implications. Rem. Sens. Environ. 82, 417–430. http://dx.doi.org/10.1016/S0034-4257(02)00057-3.
Schelde, K., Thomsen, A., Heidmann, T., Schjønning, P., 1998. Diurnal fluctuations of water and heat flows in a bare soil. Water Resour. Res. 34, 2919–2929. http://dx.doi.org/10.1029/98WR02225.
Scott, R.L., 2010. Using watershed water balance to evaluate the accuracy of eddy covariance evaporation measurements for three semiarid ecosystems. Agric. For. Meteorol. 150, 219–225. http://dx.doi.org/10.1016/j.agrformet.2009.11.002.
Scott, R.L., Edwards, E.A., Shuttleworth, W.J., Huxman, T.E., Watts, C.J., Goodrich, D.C., 2004. Interannual and seasonal variations in fluxes of water and carbon dioxide from a riparian woodland ecosystem. Agric. For. Meteorol. 122, 64–84. http://dx.doi.org/10.1016/j.agrformet.2003.09.001.
Scott, R.L., Huxman, T.E., Cable, W.L., Emmerich, W.E., 2006. Partitioning of evapotranspiration and its relation to carbon dioxide exchange in a

Chihuahuan Desert shrubland. Hydrol. Process. 20, 3227–3243. http://dx.doi.org/10.1002/hyp.6329.
Seyfried, M.S., Grant, L.E., Du, E., Humes, K., 2005. Dielectric loss and calibration of the Hydra probe soil water sensor. Vadose Zone J. 4, 1070–1079. http://dx.doi.org/10.2136/vzj2004.0148.
Smith, R.E., Chery, D.L., Renard, K.G., Gwinn, W.R., 1981. Supercritical flow flumes for measuring sediment-laden flow. U.S. Department of Agriculture Technical Bulletin 1655, Washington, DC, pp. 92.
Templeton, R.C., 2011. Insights on seasonal fluxes in a desert shrubland watershed from a distributed sensor network. MS thesis. Arizona State University, Tempe, AZ, pp. 171.
Turnbull, L., Parsons, A.J., Wainwright, J., 2013. Runoff responses to long-term rainfall variability in creosotebush-dominated shrubland. J. Arid Environ. 91, 88–94. http://dx.doi.org/10.1016/j.jaridenv.2012.12.002.
Twine, T.E., Kustas, W.P., Norman, J.M., Cook, D.R., Houser, P.R., Meyers, T.P., Prueger, J.H., Starks, P.J., Wesely, M.L., 2000. Correcting eddy-covariance flux underestimates over a grassland. Agric. For. Meteorol. 103, 279–300. http://dx.doi.org/10.1016/S0168-1923(00)00123-4.
Vachaud, G., Passerat De Silans, A., Balabanis, P., Vauclin, M., 1985. Temporal stability of spatially measured soil water probability density function. J. Soil Soc. Am. 49, 822–828.
Vivoni, E.R., 2012a. Spatial patterns, processes and predictions in ecohydrology: integrating technologies to meet the challenge. Ecohydrology 5, 235–241. http://dx.doi.org/10.1002/eco.1248.
Vivoni, E.R., 2012b. Diagnosing seasonal vegetation impacts on evapotranspiration and its partitioning at the catchment scale during SMEX04-NAME. J. Hydrometeorol. 13, 1631–1638. http://dx.doi.org/10.1175/JHM-D-11-0131.1.
Vivoni, E.R., Moreno, H.A., Mascaro, G., Rodríguez, J.C., Watts, C.J., Garatuza-Payán, J., Scott, R.L., 2008a. Observed relation between evapotranspiration and soil moisture in the North American monsoon region. Geophys. Res. Lett. 35, L22403. http://dx.doi.org/10.1029/2008GL036001.
Vivoni, E.R., Gebremichael, M., Watts, C.J., Bindlish, R., Jackson, T.J., 2008b. Comparison of ground-based and remotely-sensed surface soil moisture estimates over complex terrain during SMEX04. Rem. Sens. Environ. 112, 314–325. http://dx.doi.org/10.1016/j.rse.2006.10.028.
Vivoni, E.R., Rodríguez, J.C., Watts, C.J., 2010a. On the spatiotemporal variability of soil moisture and evapotranspiration in a mountainous basin within the North American monsoon region. Water Resour. Res. 46, W02509. http://dx.doi.org/10.1029/2009WR008240.
Vivoni, E.R., Watts, C.J., Rodríguez, J.C., Garatuza-Payán, J., Méndez-Barroso, L.A., Saiz-Hernandez, J.A., 2010b. Improved land-atmosphere relations through distributed footprint sampling in a subtropical scrubland during the North American monsoon. J. Arid Environ. 74, 579–584. http://dx.doi.org/10.1016/j.jaridenv.2009.09.031.
Wainwright, J., Parsons, A.J., Schlesinger, W.H., Abrahams, A.D., 2002. Hydrology-vegetation interactions in areas of discontinuous flow on a semi-arid bajada, southern New Mexico. J. Arid Environ. 51, 319–338. http://dx.doi.org/10.1006/jare2002.0970.
Watts, C.J., Scott, R.L., Garatuza-Payán, J., Rodríguez, J.C., Prueger, J.H., Kustas, W.P., Douglas, M., 2007. Changes in vegetation condition and surface fluxes during NAME 2004. J. Climate 20, 1810–1820. http://dx.doi.org/10.1175/JCL14088.1.
Webb, E.K., Pearman, G.I., Leuning, R., 1980. Correction of flux measurements for density effects due to heat and water vapor transfer. Quart. J. Roy. Meteorol. Soc. 106, 85–106. http://dx.doi.org/10.1002/qj.49710644707.
Wilczak, J.M., Oncley, S.P., Stage, S.A., 2001. Sonic anemometer tilt correction algorithms. Bound. Lay. Meteorol. 99, 127–150. http://dx.doi.org/10.1023/A:1018966204465.